3D nanoparticle superlocalization with a thin diffuser: supplementary information

TENGFEI WU,[1,2] MARC GUILLON,[2,3] CLEMENCE GENTNER, [1] HERVE RIGNEAULT,[4] GILLES TESSIER,[1] PIERRE BON,[5,6] PASCAL BERTO[1,3,*]

[1]Sorbonne Université, CNRS, INSERM, Institut de la Vision, 17 Rue Moreau, 75012 Paris, France
[2]Université de Paris, SPPIN – Saints-Pères Paris Institute for the Neurosciences, CNRS, 75006 Paris, France
[3]Institut Universitaire de France (IUF), Paris, France
[4]Aix Marseille Univ, CNRS, Centrale Marseille, Institut Fresnel, Marseille, France
[5]Université de Bordeaux, Laboratoire Photonique Numérique et Nanosciences, UMR 5298, 33400, Talence, France.
[6]Institut d'Optique & CNRS, LP2N UMR 5298, 33400, Talence, France.
**Corresponding author: pascal.berto@u-paris.fr*

S1: Comparison of experimental speckle and simulated speckle

This section presents a model of the complex transmission of a 1° diffuser. To this aim, we first characterized the phase-delay profile introduced by a 1° holographic diffuser (Edmund Optics) by imaging it in transmission using a commercial high-resolution wavefront sensor (PHASICS, SID4). Based on this phase measurement, we extracted a phase correlation width of w_{FWHM}=46,1 µm and a standard deviation of $\bar{\delta} = 0.156$ µm in the plane of the diffuser. We then generated numerically a pseudo-random phase mask φ_D with identical statistical properties. In practice, this phase map φ_D was generated by creating a random pixel map uniformly distributed between -1 and 1, and filtering it using a Gaussian filter|1]:

$$g(r) = \sqrt{\frac{3}{\pi}}.\frac{\bar{\delta}}{w}.e^{\frac{-r^2}{2w^2}}$$

With r the radial coordinate and $w = \frac{w_{FWHM}}{4\sqrt{\ln(2)}}$ the standard deviation of the spatial correlation.

For a thin diffuser, the angular standard deviation of the intensity per transverse dimension can be expressed as [2]:

$$\theta_0 = \frac{1}{\sqrt{2}}\frac{\bar{\delta}}{w} \approx 0.45°$$

Which leads to a scattering angle $\theta_{FWHM} = \frac{\theta_0}{\sqrt{8\ln(2)}} \approx 1.07°$ in excellent agreement with the 1° scattering angle expected for this diffuser.

As described in the main text, after interaction of a plane wave with this mask of complex transmission $D = e^{i\varphi_D}$, a Fresnel propagation computation allows to compute speckle patterns at any distance *d* from the diffuser. Figure S1(a) shows the simulated speckles at three different distances *d*. Figure S1(b) shows speckles acquired experimentally, using the 1° holographic diffuser in the corresponding conditions. Qualitatively, the three speckle patterns are indeed similar for any distance. A 1-D profile of the (2D) autocorrelation of the simulated and experimental speckles (here for d=3.9mm), shown in Fig. S1(c), confirms that the speckle grain size obtained with our procedure (FWHM~24µm) is in good agreement with the experimental one (FWHM~29µm).

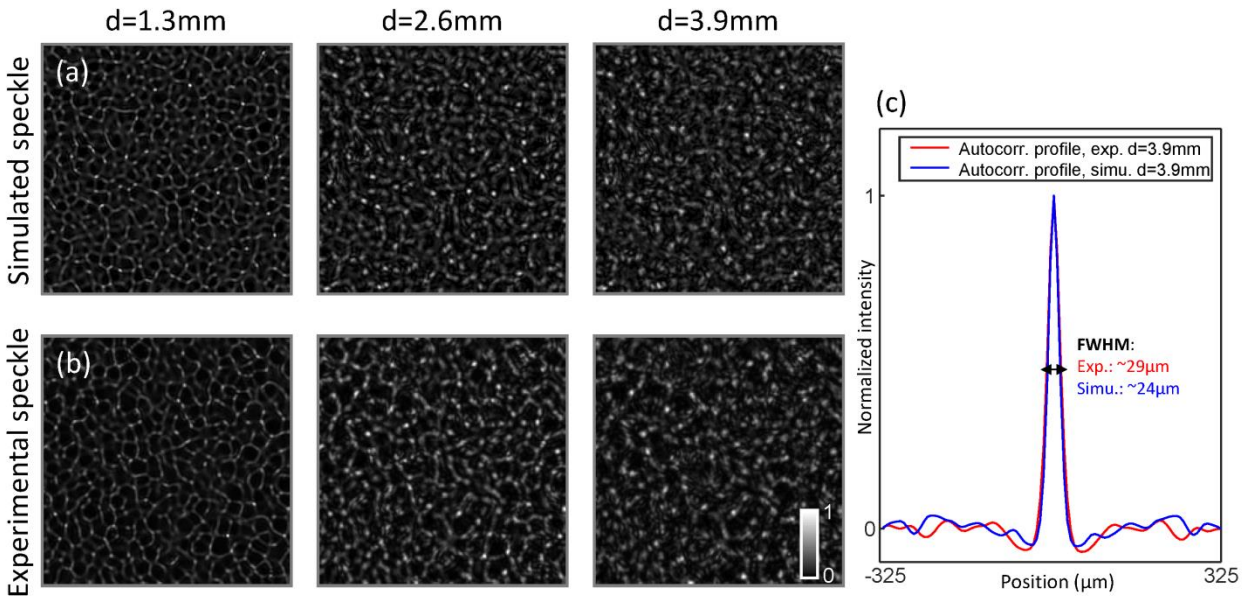

Fig. S1. Comparison of simulated and experimental speckles. (a) Simulated speckles for d=1.3mm, 2.6mm and 3.9mm. (b) Experimental speckles in the corresponding conditions. (c) Autocorrelation profiles of simulated and experimental speckles for d=3.9mm.

S2: Phase and intensity disentanglement and retrieval

Let us consider an impinging wavefield $E_{in} = \sqrt{I}e^{i\varphi}$, composed of a phase term φ (see Fig. S2(b)) and an intensity term I (see Fig. S2(c)). After propagation through the thin diffuser D, the resulting distorted speckle S_{obj} is modified in two aspects compared with the reference speckle pattern S_{ref} (planar wavefront). First, as shown in the zoomed images in Fig. S2(a), the local phase gradient of the wavefront causes local displacements $\boldsymbol{u}$ of speckle grains. Second, the intensity modulation of the impinging beam locally affects the energy in each speckle grain.

Phase and intensity entanglement: In regions of high intensity gradient, the *Demon*-based estimation of the speckle grains displacement $\boldsymbol{u}$ partially fails since the energies carried by the speckle grains in the S_{obj} and S_{ref} maps are not comparable anymore. The resulting errors in the phase gradient estimation ($\boldsymbol{\nabla}_{\perp}\varphi = k_0\boldsymbol{u}/d$) leads to strong artifacts in the reconstructed phase (see Fig. S2(d)). The most straightforward approach to retrieve intensity uses a normalization of the distorted speckle by the reference speckle. However, as can be seen in Fig. 2(e), some artifacts also occur (especially in high-phase-gradient regions, as shown in the insets). These artifacts are mainly caused by the local displacement of speckle grains $\boldsymbol{u}$ induced by a local phase gradient. Mutual errors in the phase and intensity reconstructions are clearly caused by their entanglement in the speckle pattern

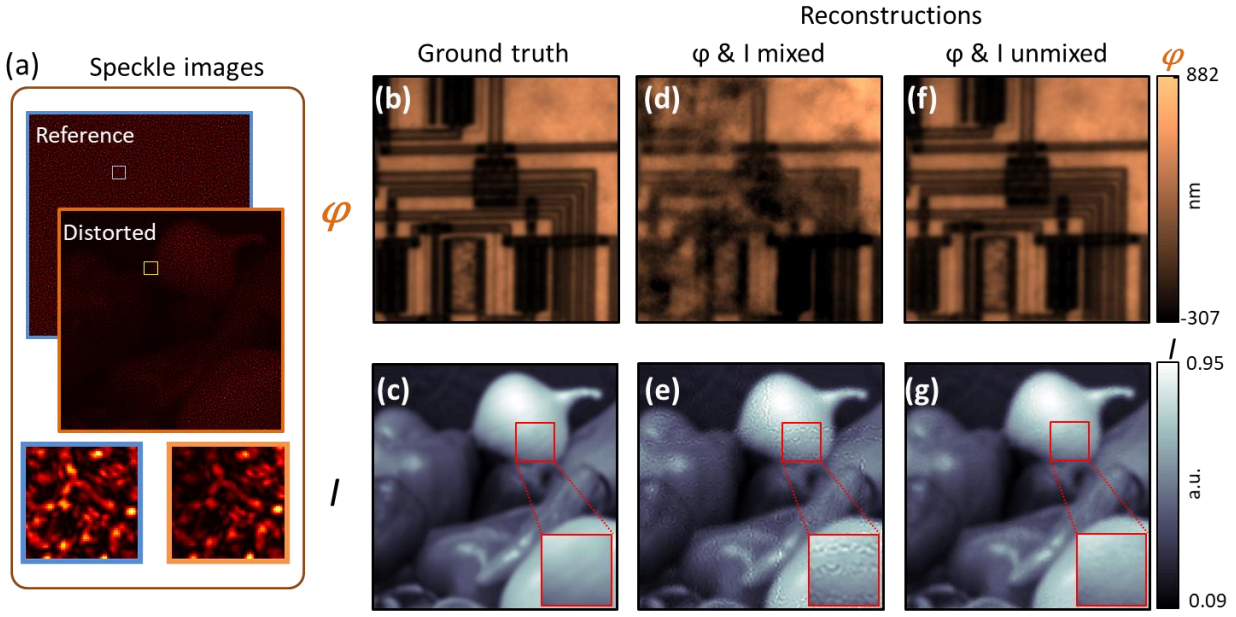

Fig. S2. Phase and intensity disentanglement for complex field retrieval (numerical simulations). (a) A reference speckle pattern (corresponding to a plane wave) is distorted when introducing both phase and intensity modulations This induces local changes in both the position and contrast of speckle grains. A complex field containing (b) a phase and (c) an intensity term is used as "ground truth". Direct reconstructions of the phase (d) and intensity (e) are affected by artifacts. The phase and intensity disentanglement method proposed in this work yields maps (f and g) which are mostly devoid of such defects.

Phase and intensity disentanglement: In Figure S3, we describe an iterative correction strategy to disentangle the phase and intensity. Here, we make use of (i) the low spatial frequency content of the speckle to retrieve the intensity pattern and (ii) the high-spatial frequency content to retrieve the displacement vector field $\boldsymbol{u}$.

First, we start by calculating a preliminary 2D map $\boldsymbol{u}$ of the speckle grain displacement between the reference $S_{ref}(r)$ and distorted $S_{obj}(r)$ speckles, using the Demon algorithm. The opposite 2D displacement map -**u** is then applied to the distorted speckle pattern. This compensates most of the local displacement of speckle grains and yields a speckle pattern $S_{obj}(r-u)$ closely approximating $S_{ref}(r)$ in terms of grain position, but not intensity. A preliminary Intensity image can therefore be estimated by normalizing the registered speckle pattern $S_{obj}(r-u)$ by the reference $S_{ref}(r)$. To minimize the effect of the registration errors and take into account the numerous dark regions of the speckle map, a regularization must be applied to retrieve the intensity modulation map $I(r)$. Here, we use a small Gaussian kernel to filter both the registered speckle and the reference before normalization. The reference speckle is finally multiplied by the estimated intensity image: $S_{ref_i+1}(r) = I(r).S_{ref_i}(r)$. In this way, we build a new reference speckle pattern S_{ref_i+1} in which speckle grains are locally comparable in intensity, but not position, to the distorted speckle S_{obj}. In a second iteration, this reference is used to re-estimate the speckle grain displacement (again using the Demon algorithm), thus providing a better estimate of **u**, and of the 2D phase gradient. After 2D integration, we finally obtain an artefact-free phase map as shown in Figure S2(g). This improved 2D local displacement map **u** can then be used to calculate an improved intensity map, as shown in the third image of Fig. S2(c). This procedure can be repeated to increase the accuracy, but two iterations typically provide sufficient accuracy, especially in the case of small displacements and weak intensity modulations.

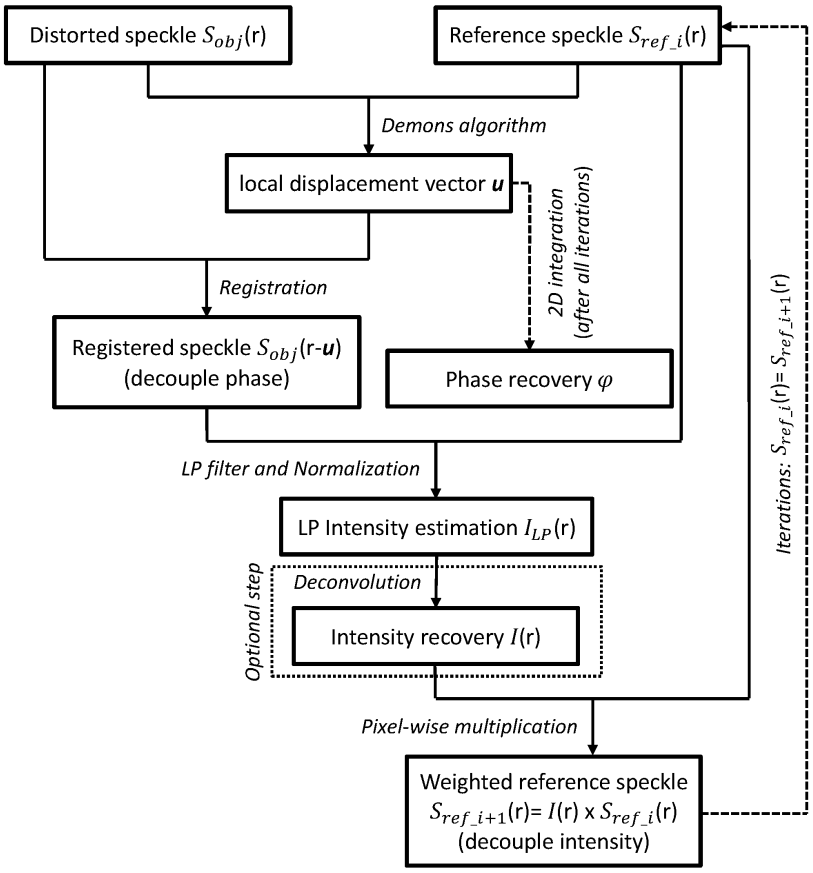

Fig. S3. Flow chart of iterative phase and intensity reconstruction from speckle patterns.

Finally, we illustrate the benefit of this iterative method when considering a simulated wavefield resulting from the interaction of light with a 100nm gold nanoparticle (NP) at a certain defocus (400nm in this example). Here, the phase shift and the intensity contrast are much weaker than for the wavefield considered in Fig. S2. However, artifacts similar to those reported above occur in both the phase and intensity recovery, as shown in Fig. S4(a and b), second column. After using the two-step local disentanglement strategy described above, both the phase and intensity reconstructions are improved (Fig. S4, third column). Although the phase is clearly improved, some differences are visible in the intensity image, due to small registration errors.

To further improve the intensity reconstruction, an additional deconvolution operation can be added to the iterative process. To achieve this, a larger smooth kernel can be applied to filter the speckle patterns before normalization, which removes most of the registration errors. A deconvolution process, considering the same known smooth kernel, finally enables a better reconstruction. A mathematical justification and an illustration of the possibilities of this deconvolution step is provided below in S3.

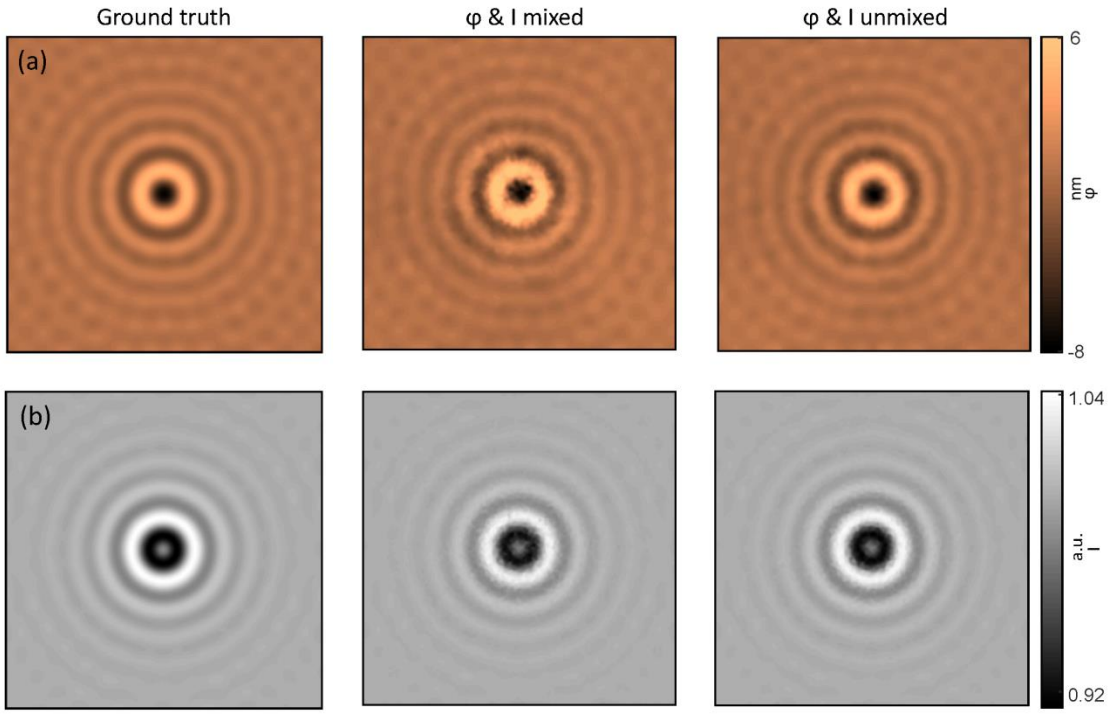

Fig. S4. Recovery of the complex field of 100nm gold NP with a thin diffuser. The ground truth of phase and intensity are respectively shown in the first column of (a) and (b). The middle column is the result before unmixing the phase and internsity in the distorted speckle pattern, and the last column shows the performance after unmixing.

S3: Intensity reconstruction: a demonstration

Here, we derive a mathematical justification for intensity modulation extraction from the low spatial frequency content of speckles pattern displayed on the camera. We assume that the transformation between the reference speckle and the distorted speckle can be written:

$$S_{obj}(r) = \left[I \times S_{ref}\right](r + u) \tag{1}$$

where r denotes the coordinates in real space and u is the displacement vector.

The object intensity I and the local speckle shift $\boldsymbol{u}$ are iteratively estimated. Their estimates are hereafter noted I' and $\boldsymbol{u'}$. Thus the registered speckle can be expressed as:

$$S_{obj}{}'(r) = \left[I' \times S_{ref}\right](r + u') \tag{2}$$

where $S_{obj}{}'$, I' and u' differ from S_{obj}, I, $\boldsymbol{u}$ due to the imperfect estimation of both speckle distortions and intensity modulation. A first order Taylor expansion of Eq. (2) in both I-I' and $\boldsymbol{u}$-$\boldsymbol{u'}$ yields:

$$S_{obj}{}'(r) \cong \left[I' \times S_{ref}\right](r + u) + (u' - u) \cdot \nabla\left[I \times S_{ref}\right](r + u) \tag{3}$$

where the term in $(u' - u)\nabla\left[(I' - I)S_{obj}\right]$ is a second order perturbation, which can therefore be neglected. Because of the gradient, the second term in Eq. (3) is dominated by high spatial frequencies. Applying a low-pass filter LP, we then get:

$$LP * S_{obj}{}'(r) \cong LP * \left[I' \times S_{ref}\right](r + u) \tag{4}$$

We now approximate that the convolution product is distributive relatively to the product so that $LP * \left(I' \times S_{ref}\right) \cong (LP * I') \times \left(LP * S_{ref}\right)$, which would be perfectly correct if S_{ref} were a grid pattern as in QLSI. In our case, this approximation holds on the fact that the spatial power spectrum of a speckle is Dirac-like at low spatial frequencies. Identifying S_{obj} and $S_{obj}{}'$, we then get:

$$LP * I' \cong \frac{LP * S_{obj}(r)}{LP * S_{ref}(r+u')} \tag{5}$$

where in practice, LP is chosen as a Gaussian kernel. From the speckle images S_{obj} and S_{ref}, one can then calculate the low-pass filtered intensity $LP * I'$ using Equation (5). We illustrate the feasibility of this operation in Fig. S5. Fig. S5(a) and S5(b) compare the result of a direct low-pass LP applied to the ground truth intensity image with that derived by Eq. (5). The difference between them is shown in Fig. S5(c): the maximum difference is only around 2.5% of the intensity contrast, which indicates that Eq. (5) LP yield similar results and have minimal influence on the final reconstruction as we show below.

We finally demonstrate that a deconvolution of the retrieved LP intensity by an appropriate Gaussian Kernel enables to retrieve the high frequency information of the intensity map I'. The Richardson-Lucy based deconvolutions are performed respectively for both cases and the corresponding results are shown in Fig. S5(d) and S5(e), which are approximated and agree well with the ground truth [Fig. S5(f)]. A further comparison is performed in Fig. S5(g), in which we plot and compare the central

profile, marked as the dashed line of Fig. S5(f). This shows that the deconvolution process enables a satisfactory intensity reconstruction.

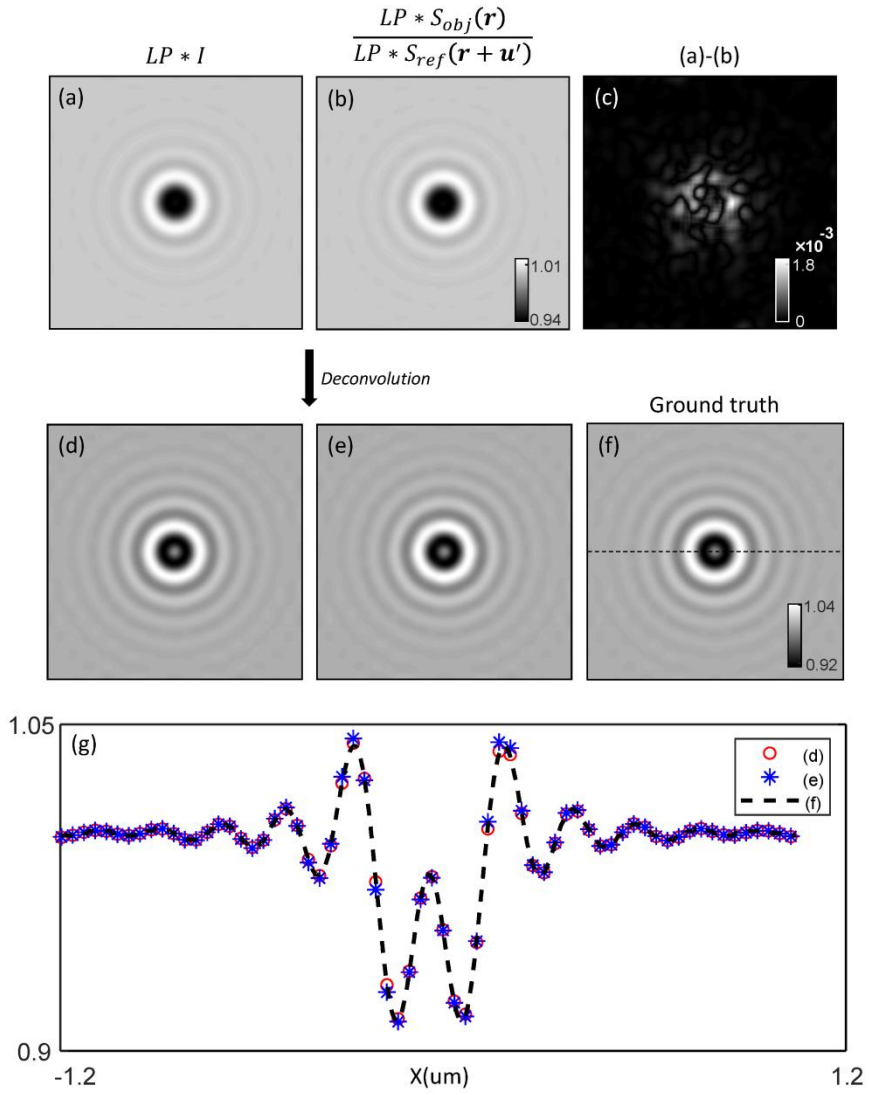

Fig. S5. Deconvolution process to recover the intensity. **(a)** Direct use of a Gaussian low-pass filter to smooth the ground truth intensity image. **(b)** Calculation using Eq. (5) **(c)** difference between images a and b. **(d)** Richardson-Lucy deconvolution of a. **(e)** deconvoution of b. **(f)** Ground truth intensity image. **(g)** profiles of d, e and f along a central line.

Supplementary S4 – Estimation of the 3D localization precision.

This section details the protocol used to estimate the 3D localization precision of the proposed approach. A series of N speckle images were collected on immobilized NPs at video rate (20Hz). For each frame, all NPs in the FOV were superlocalized to estimate their position $\mathbf{p_i}$. Although the NPs are immobilized on the coverslip, they undergo a displacement d due to mechanical drift and vibrations of the sample (see fig 3.d). For each NP, we consider that the position $\mathbf{p_i}$ is the sum of a mechanical sample displacement d, common to all objects within the field-of-view, plus a position estimation error ε_i of our approach, different for each particle. In order to estimate the accuracy of our superlocalization approach, i.e. the standard deviation of the error $\sigma(\varepsilon)$, we considered the position of 2 NPs:

$$\mathbf{p_1} = \mathbf{d} + \boldsymbol{\varepsilon_1}$$
$$\mathbf{p_2} = \mathbf{d} + \boldsymbol{\varepsilon_2}$$

To eliminate the mechanical displacement $\mathbf{d}$ and isolate the estimation error $\boldsymbol{\varepsilon_i}$ of our approach, we subtract the measured position of two NPs in the field-of-view ($\Delta\mathbf{p} = \mathbf{p_2} - \mathbf{p_1} = \boldsymbol{\varepsilon_2} - \boldsymbol{\varepsilon_1}$). Since the position measurement of each NP is affected by independent but equivalent noise distribution, the mean square fluctuations of the errors ε_i are the same for all particles, i.e. $\sigma(\varepsilon_1) = \sigma(\varepsilon_2)$, thus:

$$\sigma(\varepsilon) = \frac{\sigma(\Delta p)}{\sqrt{2}} \qquad (2)$$

For a series of N=300 speckle images, we obtained a localization precision of $\sigma_{x,y}(\varepsilon)$ =1.3nm in the lateral and $\sigma_z(\varepsilon)$=6.3nm in the axial direction when operating close to the plane of best focus.

Supplementary S5

In this section, we estimate the localization precision in 3D at different depths. To this aim, a series of displacements along the axial direction (defocus) were applied to the sample (from Δz = 0 μm to Δz = 2.6 μm in 200nm steps, with z≈0 the imaging plane of the NPs) using the piezo stage. For each NP axial position, we collected N=25 phase and intensity images using our thin-diffuser based WFS. The electromagnetic field acquired at the best focus plane were used to obtain the calibration curve by performing proper numerical propagation. By using this calibration curve and a nonlinear Levenberg–Marquardt fit, we obtained the 3D position of the nanoparticles at each depth. The localization precision at different depths, obtained using the protocol detailed in Supplementary S4, is plotted in Fig. S6. In this group of data, we obtained a precision of 7.8nm along the axial direction (Z) and 0.9nm along the lateral direction (XY) at the focal plane. At the edge of the axial range (Z=2.6μm), we obtain a localization precision of 71.0nm and 19.2nm along the axial and lateral direction respectively.

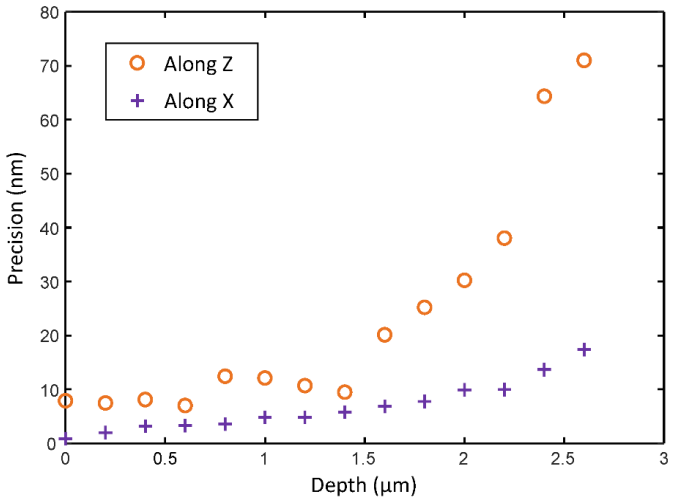

Fig. S6. Localization precision at different depths along the axial direction Z (red circle) and the lateral direction X (blue cross)

References

[1] M. Guillon, B. C. Forget, A. J. Foust, V.De Sars, M. Ritsch-Marte, and V. Emiliani, "Vortex-free phase profiles for uniform patterning with computer-generated holography," Opt. Express 25, 12640-12652 (2017)

[2] P. Arjmand, O. Katz, S. Gigan, and M. Guillon, "Three-dimensional broadband light beam manipulation in forward scattering samples," Opt. Express **29**, 6563-6581 (2021)